International Journal of Mechanical Sciences 89 (2014) 101–111

Contents lists available at ScienceDirect

International Journal of Mechanical Sciences

journal homepage: www.elsevier.com/locate/ijmecsci

Inherent and induced anisotropic finite visco-plasticity with applications to the forming of DC06 sheets

A. Behrouzi [a], C. Soyarslan [a,*], B. Klusemann [a], S. Bargmann [a,b]

[a] Institute of Continuum Mechanics and Material Mechanics, Hamburg University of Technology, Hamburg, Germany
[b] Institute of Materials Research, Helmholtz-Zentrum Geesthacht, Geesthacht, Germany

ARTICLE INFO

Article history:
Received 27 December 2013
Received in revised form
1 August 2014
Accepted 26 August 2014
Available online 3 September 2014

Keywords:
Material modeling
Plasticity
Anisotropy
Sheet metal forming
Cross hardening
IF steel

ABSTRACT

In the current work we present a finite visco-plasticity model accounting for inherent and induced plastic anisotropy as well as Bauschinger effect for the interstitial free (IF) steels and its application to a forming process simulation of DC06 sheets. The inherent plastic anisotropy uses a Hill-48 type structural tensor whereas the induced anisotropy is modeled via its evolution accounting for dynamic (active) and latent (inactive) parts. The latter appears to be an eminent requirement for predicting the qualitative effect of the evolving dislocation microstructures under orthogonal loading path changes, i.e., the cross hardening. A nonlinear isotropic and Armstrong–Frederick type kinematic hardening is also involved. Finally, the rate dependence of the plastic response is incorporated using Johnson–Cook type formulation. The model is implemented as VUMAT user defined material subroutine for ABAQUS and used in a set of sensitivity analyses to present mentioned model features. The model parameters are identified based on a set of experiments involving monotonic shear, uniaxial tension, forward to reverse shear and plane strain tension followed by shear tests. Finally, the channel forming process of a DC06 sheet is simulated. A good agreement with the experimental findings is observed, in both the tool response history curves and the extent of spring-back which is conclusive on the final product geometry.

1. Introduction

The macroscopic behavior of the polycrystalline metals is closely linked to the underlying microstructure and its evolution. Under sufficiently intense load levels, new dislocations nucleate in addition to the existing ones: they gain mobility and interact with barriers, e.g., grain boundaries, inclusions, solid solutions, as well as each other. The way how these interactions occur, depends on the loading history, i.e., the loading path being monotonic, reverse or, e.g., orthogonal. Under monotonic loading paths dislocations accumulate in front of barriers to form pile-ups. The consequent increase in the resistance to flow is referred to as strain hardening. Once the load is reversed at proceeding stages, the pile-ups are partially dissolved, with the dislocations departing from the barriers. This early re-yielding at load reversals is referred to as the Bauschinger effect [1]. On the other hand, if instead of a complete load reversal, an orthogonal loading is pursued, prevailing dislocations hinder the slip on the newly activated slip systems. Resultant latent resistance to yielding and hardening rate increase is named as cross hardening, see, e.g., Ghosh and Backofen [2] for one of the pioneering reports and Rauch and Schmitt [3] as well as Rauch and Thuillier [4] who reported dislocation microstructure alterations under tension followed by shear as subsequently orthogonal loading paths. Nesterova et al. [5] investigated the microstructure under two strain path changes (simple-shear/simple-shear and uniaxial-tension/simple-shear) in an interstitial free (IF) steel where the influence of the grain orientation is discussed as well. Gardey et al. [6] studied the dislocation structures in dual-phase steel under different loading paths, including orthogonal loading and the effect of the different strain paths on the dislocation structure is discussed in detail.

Mathematical modeling approaches associated with such micro-macro interactions differ by the scale at which the mathematical constructs and their emerging relations are formulated. The micro-scale based mechanistic approaches use mathematical entities in direct association with corresponding microstructural phenomena. Within the current context, glide-system level resolutions with crystal plasticity (e.g., [7–9] and for a recent overview see Roters et al. [10]) as well as gradient extended crystal plasticity [11–16] were presented. These approaches, while supplying higher accuracy with less approximations, require relatively high computational cost as compared to their phenomenological counterparts which base their formulations at the meso- or macroscale using smeared microstructural properties. Since the current work aims at simulation of a metal

* Corresponding author. Tel.: +49 40 42878 2562.
E-mail address: celal.soyarslan@tu-harburg.de (C. Soyarslan).

http://dx.doi.org/10.1016/j.ijmecsci.2014.08.025

forming process of DC06 steel sheets at the macroscale, a phenomenological modeling approach is adopted here.

The phenomenological approaches account for the micromechanical phenomena mentioned above through subjecting the yield surface to various transformations, such as proportional expansion, translation, rotation and distortion [17]. Standard models involving combined isotropic and kinematic hardening effects are limited to modeling only proportional expansion and translation which might not be sufficient in accurate modeling of multistage metal forming processes involving strong load path changes. Baltov and Sawczuk [18] represent one of the early works that takes into account the shape change of the yield surface during deformation known as distortional hardening. The frameworks of Baltov and Sawczuk [18], Levkovitch and Svendsen [19], Clausmeyer et al. [20], Pietryga et al. [21], Barthel et al. [22] and Barlat et al. [23] account for the texture evolution due to the interaction of dislocation structures using evolving structural tensors besides initial anisotropy and combined isotropic and kinematic hardening. The models of the Teodosiu group, e.g., [24–27] with modifications proposed by Wang et al. [28] constitute other phenomenological approaches for modeling distortional hardening effects which, as opposed to the formerly listed models, involve strong coupling between the kinematic hardening and distortional hardening formulation. This makes basic model interpretation and parameter identification relatively tough. Uenishi and Teodosiu [29] presented an extension of the previous model of the Teodosiu group to include the rate effects to describe the behavior of IF steel in crash analysis correctly. Finally, the works of Feigenbaum and Dafalias [30,31] and Plesek et al. [32] represent thermodynamically consistent distortional hardening models where the yield surface curvature at the vicinity of the loading and flattening at the opposing region can be modeled.

In the present work, following in the footsteps of the approaches proposed by Levkovitch and Svendsen [19] and Barthel et al. [22], we present a framework for rate-dependent plasticity accounting for inherent and induced plastic anisotropy as well as Bauschinger effect aiming at modeling the interstitial free (IF) steel behavior, specifically for DC06. For this purpose we devise an anisotropic yield function of Hill-48 type (cf. [33]). The fourth-order structural tensor is not taken as an invariant. However, it is assumed to evolve, where its evolution is formulated in two parts such as dynamic and latent parts in accordance with the dynamics of dislocation structures. In this way, the strength evolution associated not only with the currently active slip systems but also with the latent slip systems is taken into account, the latter of which is also known as cross hardening. The geometrical implications of the current formulation are determined by the quadratic structure of the yield locus which is preserved even during its evolution. Within this limit, e.g., rotation of the axes and the change of the aspect ratio of the ellipse representing the yield locus at the plane stress space is captured. The uniform extension of the yield locus and its shift are taken into account using a combined nonlinear isotropic and Armstrong–Frederick type kinematic hardening. This way the early re-yielding at the load reversals, i.e., the Bauschinger effect, and successive transient hardening is incorporated in the model as an eminent requirement for DC06. The IF steel DC06 is reported as the most strain rate sensitive IF steel among those being applied in automotive industries [34]. A strain rate dependent model is formulated in the current work in terms of a Johnson–Cook type formulation. The experimental curves for DC06 at different strain rates reported by van Riel [35] as well as the experimental data from [20,36,37] are used to identify the corresponding material parameters. The Teodosiu and Hu model [24] and the Levkovich model [19] both are capable of predicting the cross hardening behavior, however the strain rate effect is not included in the Levkovich model. The Teodosiu and Hu model on the other hand also considers strain rate effects however at a cost of totally 7 parameters devoted to the cross hardening (cf. [35]). In the current model, as compared to Teodosiu and Hu only 4 parameters are used for this purpose. Finally, possible change of the Young's modulus due to plastic strain or anisotropy is not accounted for in this work.

The finite strain formulation is based on a Green–Naghdi–McInnis-type hypo-elastic plastic formulation. Accordingly, additivity of the rate of deformation tensor into elastic and plastic parts is assumed. By expressing the yield function in terms of the rotated Cauchy (true) stresses the material frame indifference is naturally satisfied. The developed framework is implemented as a VUMAT user defined material subroutine for ABAQUS/Explicit. First, sensitivity analyses are performed using single finite element tests. Hereby, plane strain tension followed by simple shear and cyclic simple shear with varying amplitudes are realized in a strain controlled fashion. These analyses show that the proposed model appropriately reflects the targeted features such as cross hardening at orthogonal loading path changes, early re-yielding and transient hardening with reversed cyclic loading paths and positive rate dependence of the plastic hardening. Finally, following the corresponding material characterization studies the model is used in the simulation of a channel forming process of DC06 steel sheet. Comparisons of the simulation results with the experimental observations show very good agreement in both the tool response, i.e., the punch force demand history curve, such as the extent of the spring-back which is conclusive on the final product geometry.

The key features in the current approach can be listed as follows:

- Inclusion of rate dependence using a Johnson–Cook type formulation with parameter identification.
- Consistent implementation in ABAQUS/Explicit as VUMAT.
- Sensitivity analysis of the material model with respect to different hardening effects.
- Application of the model to an actual metal forming experimental process.

1.1. A word on notation

In the rest of the paper, the following notations will be used. Consistently assuming $\mathbf{a}$, $\mathbf{b}$, and $\mathbf{c}$ as three second-order tensors, together with the Einstein's summation convention on repeated indices, $\mathbf{c}=\mathbf{a}\cdot\mathbf{b}$ represents the single contraction product with $c_{ik}=a_{ij}b_{jk}$. $d=\mathbf{a}:\mathbf{b}=a_{ij}b_{ij}$ represents the double contraction product, where d is a scalar. $\mathbb{E}=\mathbf{a}\otimes\mathbf{b}$, $\mathbb{F}=\mathbf{a}\overline{\otimes}\mathbf{b}$, and $\mathbb{G}=\mathbf{a}\underline{\otimes}\mathbf{b}$ represent the tensor products with $E_{ijkl}=a_{ij}b_{kl}$, $F_{ijkl}=a_{ik}b_{jl}$, and $G_{ijkl}=a_{il}b_{jk}$, where $\mathbb{E}$, $\mathbb{F}$, and $\mathbb{G}$ represent fourth-order tensors. $\mathbf{a}^{\top}$ and $\mathbf{a}^{-1}$ denote the transpose and the inverse of $\mathbf{a}$, respectively. $\partial_{\mathbf{a}}\mathbf{b}$ denotes the partial derivative of $\mathbf{b}$ with respect to $\mathbf{a}$, that is $\partial\mathbf{b}/\partial\mathbf{a}$. $\mathrm{dev}(\mathbf{a})=\mathbf{a}-[1/3]\,\mathrm{tr}(\mathbf{a})\mathbf{1}$ and $\mathrm{tr}(\mathbf{a})=a_{ii}$ stand for the deviatoric part of and trace of $\mathbf{a}$, respectively, $\mathbf{1}$ denoting the identity tensor. $\mathrm{sym}(\mathbf{a})$ and $\mathrm{skw}(\mathbf{a})$ denote symmetric and skew-symmetric portions of $\mathbf{a}$. $\dot{\mathbf{a}}$ gives the material time derivative of $\mathbf{a}$. $\langle x\rangle=[1/2][x+|x|]$ describes the ramp function. The norm of $\mathbf{a}$ is denoted by $|\mathbf{a}|=\sqrt{\mathbf{a}:\mathbf{a}}$. Finally, $\widehat{\mathbf{a}}$ is the rotationally neutralized representation of $\mathbf{a}$.

2. Theory

2.1. Material model – small strain formulation

We set the stage by assuming the additivity of the total strain tensor $\mathbf{E}$ into elastic $\mathbf{E}^e$ and plastic $\mathbf{E}^p$ parts viz.

$$\mathbf{E}=\mathbf{E}^e+\mathbf{E}^p. \tag{1}$$

The stress tensor $\mathbf{S}$ is computed from the quadratic elastic strain energy $\Psi^e=[1/2][\mathbf{E}^e:\mathbb{C}:\mathbf{E}^e]$ with $\mathbb{C}^e$ denoting the elastic

constitutive tensor with

$$\mathbb{C}^e := \left[\kappa - \frac{2\mu}{3}\right][\mathbf{1}\otimes\mathbf{1}] + \mu[\mathbf{1}\overline{\otimes}\mathbf{1} + \mathbf{1}\underline{\otimes}\mathbf{1}], \tag{2}$$

where κ and μ are the elastic bulk and the shear moduli, respectively, which are treated as constants. Hence, the time rate of change of $\mathbf{S}$ reads

$$\dot{\mathbf{S}} = \mathbb{C} : \dot{\mathbf{E}}^e = \kappa\,\mathrm{tr}(\dot{\mathbf{E}}^e)\mathbf{1} + 2\mu\,\mathrm{dev}(\dot{\mathbf{E}}^e). \tag{3}$$

The material behavior of polycrystalline sheet metals during forming processes is predominantly determined by a changing dislocation microstructure and attendant evolving anisotropic yield behavior. In addition to the shift of the yield surface and its proportional expansion as in the case of conventional combined hardening, the current model also accounts for an evolving yield surface shape, i.e., cross hardening. Under these effects the plastic flow potential ϕ^p is represented by

$$\phi^p := \sqrt{[\sigma_{\mathrm{eq}}]^2 + [\mathbf{S}-\mathbf{X}] : [\mathbb{H}] : [\mathbf{S}-\mathbf{X}]} - \sigma_y(e^p, \dot{e}^p) \le 0, \tag{4}$$

Here, σ_{eq} denotes an equivalent stress measure of any kind, e.g., Hill-48 [33], Hosford [38], Karafillis and Boyce [39], or Barlat [40]. Since in the current application a Hill-48 type initial anisotropy is aimed at, we make use of $[\sigma_{\mathrm{eq}}]^2 = [\mathbf{S}-\mathbf{X}] : [\mathbb{A}] : [\mathbf{S}-\mathbf{X}]$. Thus, Eq. (4) is rearranged to give

$$\phi^p := \sqrt{[\mathbf{S}-\mathbf{X}] : [\mathbb{A}+\mathbb{H}] : [\mathbf{S}-\mathbf{X}]} - \sigma_y(e^p, \dot{e}^p) \le 0, \tag{5}$$

In the above the initial (Hill-48-type) and the evolving fourth-order flow anisotropy tensors are, respectively, denoted by $\mathbb{A}$ and $\mathbb{H}$. $\mathbf{X}$ is the back stress tensor. $\sigma_y(e^p, \dot{e}^p)$ denotes the flow stress accounting for the isotropic hardening of the material with strain and strain rate effects. Hence, letting e^p denote the equivalent plastic strain and $\dot{e}^p$ its rate, $\sigma_y(e^p, \dot{e}^p)$ follows a Johnson–Cook type, [41], multiplicative form in which thermal effects are omitted

$$\sigma_y(e^p, \dot{e}^p) := h_y(e^p) r_y(\dot{e}^p). \tag{6}$$

Here, $h_y(e^p)$ and $r_y(\dot{e}^p)$ denote the functions of strain hardening and strain rate hardening which are defined as

$$\left.\begin{aligned} h_y(e^p) &:= b - [b - \sigma_{y0}]\exp(-m[e^p]^n), \\ r_y(\dot{e}^p) &:= 1 + c\log(\dot{e}^p/\dot{e}_0^p), \end{aligned}\right\} \tag{7}$$

where σ_{y0}, b, c, n and m are material parameters. The reference rate is denoted by $\dot{e}_0^p$. During fully developed plastic flow the consistency condition is satisfied, i.e., $\dot{\phi}^p = 0$. Hence, the current visco-plastic formulation is referred to as a consistency type visco-plastic formulation, see, e.g., [42]. Thus, the proposed model is capable of reflecting strain rate effects in contrast to similar models, e.g., [19,20].

An associative form is selected for the evolution of the plastic flow

$$\dot{\mathbf{E}}^p/\dot{e}^p = \partial_{\mathbf{S}}\phi^p = \frac{[\mathbb{A}+\mathbb{H}] : [\mathbf{S}-\mathbf{X}]}{\sqrt{[\mathbf{S}-\mathbf{X}] : [\mathbb{A}+\mathbb{H}] : [\mathbf{S}-\mathbf{X}]}}. \tag{8}$$

For definition of the equivalent plastic strain rate, following [43] we define the rate of plastic work $\dot{w}^p$ as

$$\dot{w}^p = \mathbf{S} : \dot{\mathbf{E}}^p = \underbrace{[\mathbf{S}-\mathbf{X}] : \dot{\mathbf{E}}^p}_{=:\dot{w}^p_{\mathrm{stationary}}} + \underbrace{\mathbf{X} : \dot{\mathbf{E}}^p}_{=:\dot{w}^p_{\mathrm{translation}}}. \tag{9}$$

Using Hill-48 type σ_{eq}, $[\mathbf{S}-\mathbf{X}] : [\mathbb{A}+\mathbb{H}] : [\mathbf{S}-\mathbf{X}]$ is degree-one homogeneous with respect to $[\mathbf{S}-\mathbf{X}]$. Thus, substituting Eq. (8) into Eq. (9), with an abuse of notation $\sigma_y = \sigma_y(e^p, \dot{e}^p)$, one has

$$\dot{w}^p_{\mathrm{stationary}} = [\mathbf{S}-\mathbf{X}] : \dot{\mathbf{E}}^p = \dot{e}^p \frac{[\mathbf{S}-\mathbf{X}] : [\mathbb{A}+\mathbb{H}] : [\mathbf{S}-\mathbf{X}]}{\sqrt{[\mathbf{S}-\mathbf{X}] : [\mathbb{A}+\mathbb{H}] : [\mathbf{S}-\mathbf{X}]}} = \dot{e}^p\sigma_y. \tag{10}$$

Hence,

$$\dot{e}^p = \frac{[\mathbf{S}-\mathbf{X}] : \dot{\mathbf{E}}^p}{\sigma_y}. \tag{11}$$

The kinematic hardening behavior is modeled via a variant of the Armstrong–Frederick form

$$\dot{\mathbf{X}}/\dot{e}^p = c_x[s_x\mathbf{N}^p - \mathbf{X}], \tag{12}$$

where c_x and s_x are associated with the saturation rate and magnitude with the back stress tensor $\mathbf{X}$, respectively. $\mathbf{N}^p$ denotes the unit direction of the inelastic deformation with $\mathbf{N}^p = \dot{\mathbf{E}}^p/|\dot{\mathbf{E}}^p|$ where $\mathbf{N}^p : \mathbf{N}^p = 1$.

The evolution of the flow anisotropy tensor determines the shape changes in the yield surface due to the microstructure evolution and is modeled introducing the following evolutionary relation (see, e.g., [19])

$$\dot{\mathbb{H}}/\dot{e}^p = c_d[s_d\mathbf{N}^p \otimes \mathbf{N}^p - \mathbb{H}^d] + c_l[s_l[\mathbf{N}^p \otimes \mathbf{N}^p - \mathbb{I}^{\mathrm{dev}}] - \mathbb{H}^l], \tag{13}$$

where $\mathbb{I}^{\mathrm{dev}}$ is the deviatoric part of the fourth-order symmetric identity tensor, $\mathbb{I}^{\mathrm{sym}} = [1/2][\mathbf{1}\overline{\otimes}\mathbf{1} + \mathbf{1}\underline{\otimes}\mathbf{1}]$, with $\mathbb{I}^{\mathrm{dev}} = \mathbb{I}^{\mathrm{sym}} - [1/3][\mathbf{1}\otimes\mathbf{1}]$. The projections of $\mathbb{H}$ parallel and orthogonal to $\mathbf{N}^p$ are, respectively, denoted by $\mathbb{H}^d = [\mathbf{N}^p : \mathbb{H} : \mathbf{N}^p][\mathbf{N}^p \otimes \mathbf{N}^p]$ and $\mathbb{H}^l = \mathbb{H} - \mathbb{H}^d$. This form is based on the idea of growth and saturation of the dynamic ($\mathbb{H}^d$) and latent ($\mathbb{H}^l$) parts of the flow anisotropy tensor $\mathbb{H}$. Here, c_d and s_d represent the saturation rate and magnitude associated with $\mathbb{H}^d$, respectively. Analogously, c_l and s_l are the saturation rate and magnitude associated with $\mathbb{H}^l$, respectively.

2.2. Extension to finite strains

Let $\mathbf{X}$ and $\mathbf{x} := \boldsymbol{\varphi}(\mathbf{X}, t)$ denote the particle positions at the reference (undeformed) configuration Ω_0 and current (deformed) configuration Ω, respectively. $\mathbf{F} := \partial_{\mathbf{X}}\boldsymbol{\varphi}(\mathbf{X}, t)$ defines the deformation gradient of the nonlinear map $\boldsymbol{\varphi} : \Omega_0 \times \mathbb{R} \to \mathbb{R}^3$. Any infinitesimal material vector $d\mathbf{X}$ at the reference configuration is transformed to its final setting $d\mathbf{x}$ at the current configuration via

$$d\mathbf{x} := \mathbf{F} \cdot d\mathbf{X}. \tag{14}$$

where the multiplicative kinematic split of the deformation gradient into elastic and plastic parts is used, viz.

$$\mathbf{F} := \mathbf{F}^e \cdot \mathbf{F}^p, \tag{15}$$

Letting $\mathbf{l} := \dot{\mathbf{F}} \cdot \mathbf{F}^{-1} = \partial_{\mathbf{x}}\mathbf{v}$ denote the spatial velocity gradient, with $\mathbf{v} = \dot{\mathbf{x}}$, and noting that $\dot{\mathbf{F}} = \dot{\mathbf{F}}^e \cdot \mathbf{F}^p + \mathbf{F}^e \cdot \dot{\mathbf{F}}^p$ and $[\mathbf{F}]^{-1} = [\mathbf{F}^p]^{-1} \cdot [\mathbf{F}^e]^{-1}$, one has

$$\mathbf{l} = \dot{\mathbf{F}}^e \cdot \mathbf{F}^p \cdot [\mathbf{F}^p]^{-1} \cdot [\mathbf{F}^e]^{-1} + \mathbf{F}^e \cdot [\mathbf{F}^e]^{-1}. \tag{16}$$

Defining $\mathbf{l}^e := \dot{\mathbf{F}}^e \cdot [\mathbf{F}^e]^{-1}$, and $\mathbf{l}^p := \dot{\mathbf{F}}^p \cdot [\mathbf{F}^p]^{-1}$, one reaches

$$\mathbf{l} = \mathbf{l}^e + \mathbf{F}^e \cdot \mathbf{l}^p \cdot [\mathbf{F}^e]^{-1}. \tag{17}$$

For the metallic materials of interest the range of elastic strains falls far below the range of plastic ones. As a consequence, the small elastic strain assumption, i.e., $\mathbf{F}^e \approx \mathbf{1}$, supplies $\mathbf{l} = \mathbf{l}^e + \mathbf{l}^p$. The symmetric part of $\mathbf{l}$ gives the spatial rate of deformation tensor $\mathbf{d} := \mathrm{sym}(\mathbf{l})$. One finally reaches the following additive split from a multiplicative split:

$$\mathbf{d} = \mathbf{d}^e + \mathbf{d}^p, \tag{18}$$

with $\mathbf{d}^e := \mathrm{sym}(\mathbf{l}^e)$, $\mathbf{d}^p := \mathrm{sym}(\mathbf{l}^p)$. This forms the basis of hypoelastic–plastic formulations which rely on certain objective rates of the selected stress measures. ABAQUS/VUMAT convention uses the Green–Naghdi–McInnis rate of the Cauchy (true) stress $\boldsymbol{\sigma}$ which requires the rotationally neutralized rate of deformation tensor $\hat{\boldsymbol{\epsilon}}$

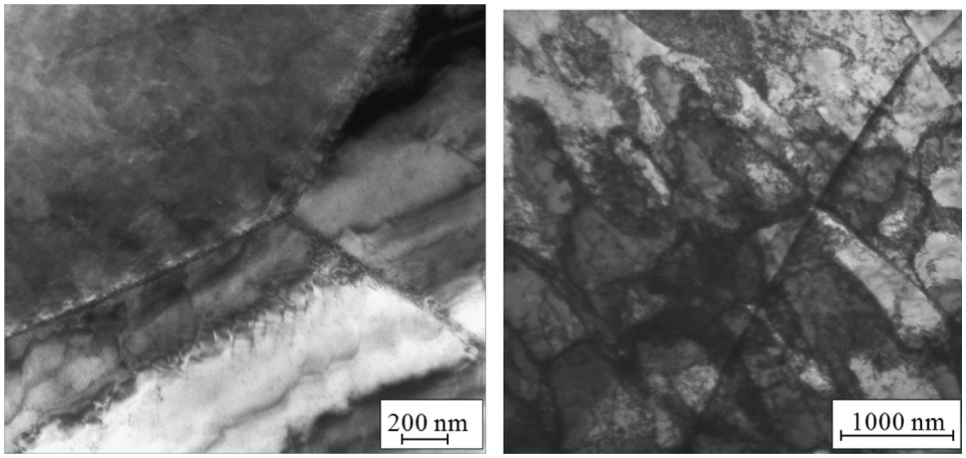

Fig. 1. TEM-images of DC06. Left: initial state. Grain boundaries at the triple point are clearly visible. Right: dislocations structure after 5% uniaxial tension. Cell walls inside a grain can be seen. Courtesy of G. Gerstein, University of Hanover, Germany.

which is defined as

$$\hat{\dot{\boldsymbol{\epsilon}}} = \mathbf{R}^{\top} \cdot [\mathbf{d}^{e} + \mathbf{d}^{p}] \cdot \mathbf{R} = \hat{\dot{\boldsymbol{\epsilon}}}^{e} + \hat{\dot{\boldsymbol{\epsilon}}}^{p}, \tag{19}$$

with $\hat{\dot{\boldsymbol{\epsilon}}}^{e} := \mathbf{R}^{\top} \cdot \mathbf{d}^{e} \cdot \mathbf{R}$, $\hat{\dot{\boldsymbol{\epsilon}}}^{p} := \mathbf{R}^{\top} \cdot \mathbf{d}^{p} \cdot \mathbf{R}$. Here, $\mathbf{R}$ denotes the rotation tensor, carried out by the polar decomposition of the deformation gradient, $\mathbf{F} := \mathbf{R} \cdot \mathbf{U}$, with $\mathbf{U}$ representing the symmetric right stretch tensor. Similarly, a pull back operation on the Cauchy (true) stress tensor $\boldsymbol{\sigma}$ with the rotation tensor gives its rotationally neutralized counterpart viz $\widehat{\boldsymbol{\sigma}} := \mathbf{R}^{\top} \cdot \boldsymbol{\sigma} \cdot \mathbf{R}$ whose material time derivative $\hat{\dot{\boldsymbol{\sigma}}}$ can be objectively integrated. Hence, the finite strain extension of the presented framework is simply realized using the replacements $\dot{\mathbf{S}} \longrightarrow \hat{\dot{\boldsymbol{\sigma}}}$ and $\dot{\mathbf{E}} \longrightarrow \hat{\dot{\boldsymbol{\epsilon}}}$ and representing the expressions at the rotationally neutralized configuration.

The developed material model is implemented as an ABAQUS/VUMAT subroutine[1] and used in the simulations given in the subsequent sections. The details of the implementation using the Voigt notation can be found in the Appendix.

3. Parameter identification for DC06

Cold-rolled steel sheet DC06 is an interstitial free steel type commonly applied for forming processes. Many difficult automotive parts such as oil pans, side panels and interior door parts are manufactured through forming DC06 sheets. As DC06 shows high strain path sensitivity, it is known as a material with a complex anisotropic hardening behavior. The evolution of dislocation microstructure during plastic deformation determines the hardening behavior of this material. A cellular structure is formed by dislocations after inducing plastic deformation and the dislocation density will increase at the cell boundaries when more plastic strain is induced. The microstructural evolution of a DC06 sample under uniaxial tensile deformation (captured by TEM) is shown in Fig. 1. Cross hardening is one of the observed hardening modes of this material that evolves during orthogonal loading path changes. This phenomenon is dominated by the evolutionary changes in dislocation microstructures. In general, such phenomena are not captured in classical material models. As a consequence, materials like DC06, that show complex microstructure behavior, are challenging ones to predict the material behavior correctly. The DC06 sheets used in this study are prepared by cold rolling followed by annealing and finishing by skin pass process. The steel sheets in this work are of 1.0 mm thickness and provided and chemically analyzed by ThyssenKrupp Steel Europe AG; see Table 1 (cf. [20,36]). The material specifications are obtained from the performed test on the DC06 sheet. The average Lankford's coefficients in 0°, 45° and 90° with respect to the rolling direction are determined as $r_0 = 2.31$, $r_{45} = 1.95$ and $r_{90} = 2.77$, respectively [20]. Their relation with the Hill-48 constants, F, G, H, L, M, and N are given as follows:

$$F = \frac{r_0}{r_{90}[1+r_0]}, \quad G = \frac{1}{[1+r_0]}, \quad H = \frac{r_0}{[1+r_0]}, \quad L = \frac{1}{2}\frac{[r_0+r_{90}][1+2r_{45}]}{r_{90}[1+r_0]}. \tag{20}$$

with $M = N = L$.

To identify the material parameters in the formulated material model, experimental data for monotonic shear, uniaxial tension, forward to reverse shear and plane strain tension followed by shear tests are used (cf. [20,35–37]). The simple shear tests and the combined plane strain tension to shear tests were conducted on a biaxial tester (equipped with two axes which can be moved independently) at Applied Mechanics Group, Faculty of Engineering Technology, University of Twente, Netherlands (cf. [44,35]).

The isotropic strain hardening parameters in the Johnson–Cook model (σ_{y0}, b, m and n) in Eq. (7) are identified based on the monotonic shear and the plane strain tension results. The plane strain tension followed by shear test is used to identify the model parameters associated with cross hardening (s_d, c_d, s_l and c_l). The simulation results of the presented model are compared with the experimental data for monotonic shear and the plane strain tension followed by the shear tests in Fig. 2. The Frederick–Armstrong kinematic hardening parameters are adopted as the ones in Clausmeyer et al. [20].

The strain rate hardening parameters in Johnson–Cook model ($\dot{\epsilon}_0^p$ and c) in Eq. (7) are identified using the experimental stress–strain curves represented in van Riel [35] for the strain rates $\dot{\epsilon} = [0.005\ \mathrm{s}^{-1}, 0.011\ \mathrm{s}^{-1}, 0.065\ \mathrm{s}^{-1}]$. The reference strain rate parameter $\dot{\epsilon}_0^p$ is identified to be $0.005\ \mathrm{s}^{-1}$ and the strain rate sensitivity parameter c as 0.0857. In Fig. 3 the strain rate sensitivity of the model is compared to the corresponding experimental curves in plane strain tensile loading [35]. The identified material parameters for DC06 are summarized in Table 2.

4. Applications

In order to assess the presented material model two sets of numerical simulation have been used. First, in a one element test the capability of the model in capturing different aspects of

[1] Interested reader can access the developed user defined material subroutine (VUMAT) by sending a request to the e-mail address of the corresponding author.

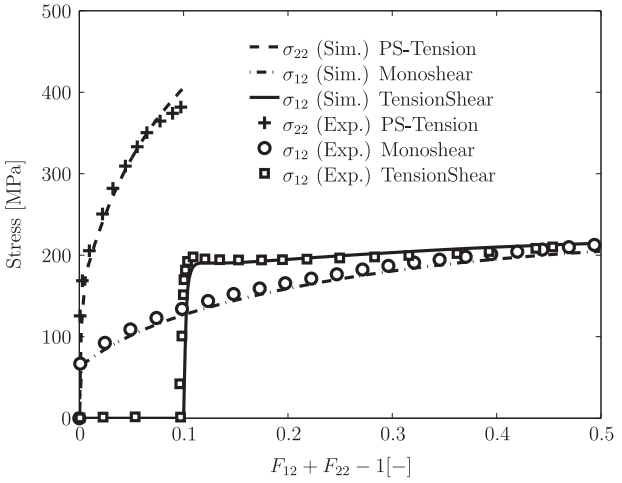

Fig. 2. Comparison of the model response to the monotonic shear test and the plane strain tension followed by shear test with the experiments data from [35,20].

Table 1
Chemical composition of DC06. All values are given as multiples of 10^{-5} mass fraction. The data set is determined by ThyssenKrupp Steel Europe AG [20,36].

Alloying component	C	Si	Mn	P	S	Al	N	Ti
10^{-5} mass fraction	3	18	137	13	10	35	2.7	79

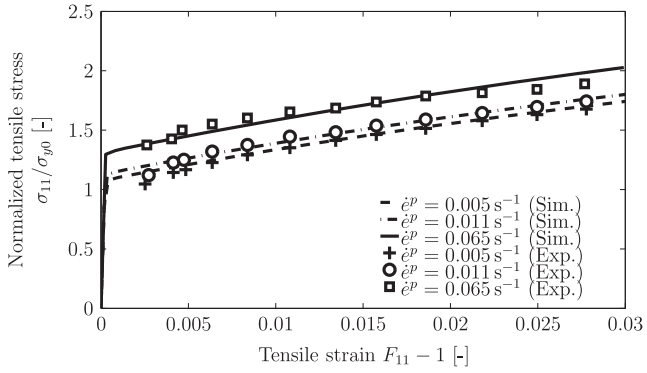

Fig. 3. Identification of strain rate sensitivity in Johnson–Cook model using the experimental results represented in [35].

material hardening under strain path changes is investigated. The response of each single hardening mode in terms of a sensitivity analysis is represented at first.

Afterwards, by simulation of an experimentally performed drawing process, the applicability of the model to industrial problems is tested. The description and results of each case study are represented in the next subsections.

4.1. Single element tests and sensitivity analyses

The one element tests are performed with a cubic 8 node element C3D8 (C3D8) (in other words please put C3D8 in bracets) with unit size. To concentrate on the effect of the induced anisotropy only, an initial yield surface of von-Mises type is assumed in this section. Three sets of numerical tests are performed to investigate the models performance. First, the simulations are run for a combined plane strain tension and simple shear loading path. The displacement in the x-direction is constrained and the uniaxial displacement in the y-direction is applied in the plane strain load case. The simple shear loading is examined by inducing the shear deformation in the

Table 2
Identified material parameters for interstitial free DC06. Parameter values determined from uniaxial tension, monotonic shear, cyclic shear, and orthogonal tension-shear experimental test data, see [44,20].

Parameter	Symbol	Value	Unit
Elastic constants	κ	150.833	GPa
	μ	69.615	GPa
Johnson–Cook constants	σ_{y0}	108.0	MPa
	b	320.0	MPa
	m	7.60	
	n	1.18	
	$\dot{\epsilon}_0^p$	0.005	s^{-1}
	c	0.086	
Hill-48 constants	F	0.252	
	G	0.302	
	H	0.698	
	L	1.357	
	M	1.357	
	N	1.357	
Kinematic hardening constants	s_x	56.0	MPa
	c_x	33.1	
Cross hardening constants	s_d	0	
	c_d	23.90	
	s_l	0.83	
	c_l	87.30	

xy-plane. The effect of each single hardening mode (isotropic, kinematic and cross) as well as combinations of them are presented in Figs. 4 and 5. For this purpose, single hardening modes are turned off by setting the corresponding material parameters accordingly.

The Cauchy shear stress component σ_{12} versus the sum of the deformation gradient components $F_{11}+F_{12}-1$ is depicted in Fig. 4. The share of each hardening mode is clearly observable. In addition, the Cauchy stress component σ_{22} during the considered loading path is shown in Fig. 5.

The results show that the isotropic, kinematic and cross hardening contributions are accounted for in the proposed model formulation. In the first part of the loading path (plane strain tension), the full model (Iso+Kin+Cro) yields the same stress response as combined isotropic and kinematic hardening (Iso+Kin). As expected, the cross hardening mode does not contribute to the stress in the first part of the applied loading path. Conversely, a significant stress overshoot in the Cauchy stress component σ_{12} is observable in the full hardening model at the beginning of simple shear loading (cf. Fig. 4). This is not captured in the combined isotropic and kinematic hardening model due to the evolved cross hardening. The Bauschinger effect and its saturation at higher strain amplitudes are observable.

To illustrate the effect of kinematic hardening in more detail, the model is analyzed for three simple shear loading cycles of different strain amplitudes as shown in Fig. 6. The Bauschinger effect, i.e., a reduction of the yield stress after reversal loading, is clearly observed.

In addition to the obtained results for DC06, further numerical investigations of the proposed model with different set of model parameters associated with flow anisotropy tensor have been performed. The results showed that a wide range of cross hardening sensitivity was covered by the model. The results of the sensitivity analysis with respect to the magnitude of the latent hardening part s_l under plane strain followed by simple shear loading are shown in Fig. 7. The represented curves in this figure show the material response in the plane strain loading followed by the simple shear loading for the different values of s_l parameter.

The results show the flexibility of the material model in reflecting the cross hardening behavior in other materials with different sensitivities to load path changes.

The capability of the material model to predict the evolving yield surface in the considered loading path is demonstrated in Fig. 8a and b. The evolution of yield surface at the end of each part of loading path as well as its initial state is depicted in Fig. 8a for the full hardening model. Comparing the yield surface at the end of plane strain tension with the initial yield surface clearly shows the shift of the center due to the kinematic hardening. The cross hardening effect is reflected in this figure through orientation change of the yield surface. The change in the aspect ratio of the yield surface is observable as well. According to the definition of the cross hardening part in the formulation of the material model, it is expected to see the expansion of yield surface in the parallel and perpendicular directions respect to the loading direction due to the dynamic and latent parts of induced anisotropy, respectively. In the first loading phase (plane strain tension), the projection of loading direction on the major axis of the yield ellipse is greater than that on the minor axis. In this regard, if we focus on the contribution of the cross hardening mode, the expansion of the yield surface toward its minor axis is mainly the effect of the latent part. In the second loading path, the direction of loading is toward the minor axis of the initial yield surface and the effect of the latent part due to cross hardening is the growth of the yield surface in the direction of the major axis of initial yield surface. The growth of the yield surface in this direction at the end of second part of the loading path is clearly observable in Fig. 8a, as anticipated. Finally, inspecting the normals to the yield loci at uniaxial stress points, the evolution of the in-plane anisotropy, i.e., the Lankford's coefficients, is observable.

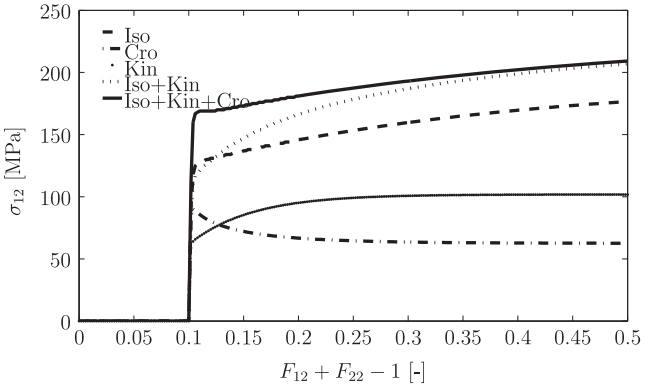

Fig. 4. Plane strain tension followed by simple shear test. Cauchy stress σ_{12} versus sum of deformation gradient components $F_{11}+F_{12}-1$ for different hardening contributions active: Iso, Kin and Cro refer to isotropic, kinematic, and cross hardening, respectively.

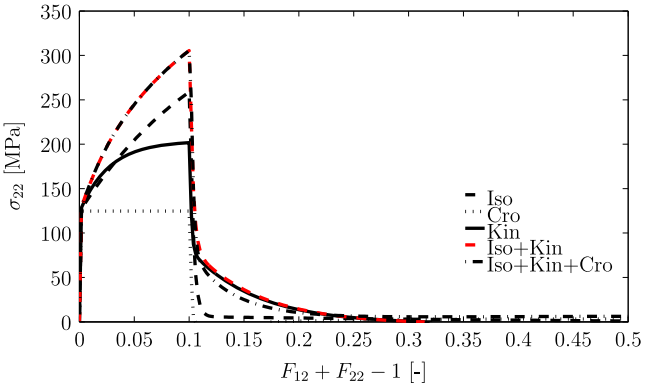

Fig. 5. Plane strain tension followed by simple shear test. Cauchy stress σ_{22} versus strain $F_{12}+F_{22}-1$ for different hardening contributions active. As expected, cross hardening does not play a role. Iso, Kin and Cro refer to isotropic, kinematic, and cross hardening, respectively.

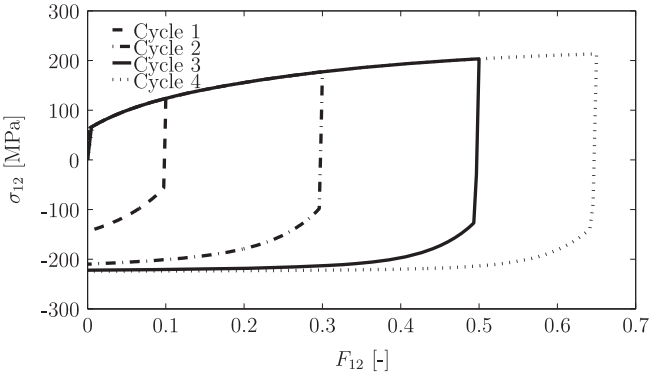

Fig. 6. Three simple shear loading cycles with different strain amplitudes. Cauchy stress component σ_{12} versus strain F_{12}. The Bauschinger effect and its saturation are observable.

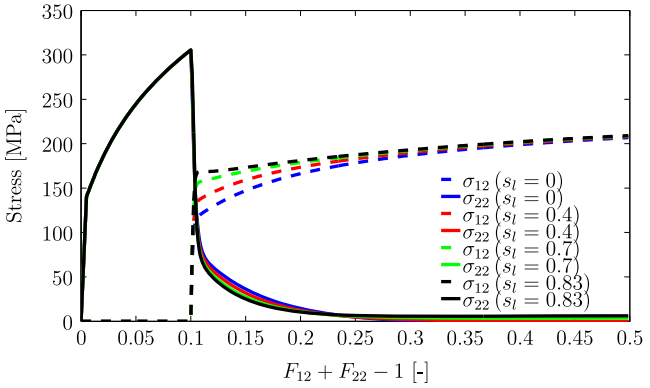

Fig. 7. Sensitivity analysis with respect to s_l for the plane strain tension followed by the simple shear loading (σ_{11}, σ_{22} and σ_{12} versus strain $F_{12}+F_{22}-1$).

To investigate the effect of cross hardening to the yield surface evolution, the yield surface at the end of the first part of loading path (plane strain tension) is plotted in Fig. 8b for two combination of hardening modes: one for the complete model considering the effect of isotropic, kinematic and cross hardening and the other without the cross hardening contribution. Both combinations predict the same yield points on the loading path. That is in agreement with the depicted curves in Fig. 5 for the first part of the loading path. Moreover, the effect of cross hardening in determining the orientation and the expansion of yield surface is obviously reflected in this figure. Further, it is seen for a following orthogonal loading path, the full model predicts higher yield that is in accordance with the shear stress curve in Fig. 4 at the beginning of the simple shear loading. Accordingly, the latent slip system orthogonal to the current loading direction is taken into account in the proposed model. In addition, to reflect the cross hardening effect in predicting the yield surface, the investigation of the yield surface evolution after orthogonal loading change shows that the orientation of the yield surface returns to its initial one after a slight loading. Further, shear loading results in the expansion of the yield surface in this orientation (cf. Fig. 8a). According to the above results, the introduced model captures all the target features well, but the feasibility investigation of the model for the real sheet forming process remains – this is done in the following.

4.2. An industrial process simulation

An open section channel (cf. Fig. 9) is selected for the experimental drawing process and the results are recorded to verify the simulation results. As the selected geometry comprises different complex curves, different plastic strain paths occur in different zones of the DC06 sheet during the forming process. Consequently, the various hardening modes such as isotropic, kinematic and cross hardening take part during the deformation. The forming processes were performed at the Institute of Forming Technology and Lightweight Construction, Technical University of Dortmund, Germany, on a double acting hydraulic press with maximum 1000 kN capacity. The die components comprising punch, matrix and blank-holder are made of tool steel C60 according to DIN EN 10027-2. The blank-holder force is provided hydraulically at the constant value of 200 kN during loading step. However, due to the hydraulic oscillation, this was not completely achieved (see Fig. 10). Contacting surfaces are covered by a lubrication formulated on solvent renewed mineral oil with a viscosity of 67 mm^2/s at 40 °C. To determine the Coulomb friction coefficient, the contact conditions in the channel forming process are simulated in several simple experimental tests (cf. [45]). For each contact test, rectangular metal strips (300 mm × 400 mm) are prepared and lubricated corresponding to the contact conditions of the considered contact set. The prepared strips are pressed against each other with a definite force and the required pulling force for each test is measured. The friction coefficient has experimentally been identified as $\mu = 0.15$. During the forming process, the die displacement, the blank-holder force and the force acting on the die are recorded with a frequency of 50 Hz. For homogeneous load distribution, avoiding dynamic effect and geometry precision, the forming process is performed at the low loading rate of about 4 mm/s. Moreover, the final geometry is measured by ATOS machine to compare to the obtained final geometry from process simulation. Three tests with the identical conditions are carried out to check the test repeatability. Comparing the force-time recorded results and the final geometry of workpiece obtained from each repetition shows no considerable differences.

In the following, the above experimental forming process is modeled and the numerical results are compared to the experimental data. The meshed parts of the channel forming process in the simulation are shown in Fig. 11. The die parts are meshed by rigid shell elements R3D4 and the blank is meshed by 8-node elements C3D8R with reduced integration and 1 mm approximate element size. Five layers of elements are used with the total number of 75,030 elements for the blank mesh. The simulation is performed as Explicit using a VUMAT subroutine in ABAQUS/Explicit. The initial anisotropy is considered using the Hill-48 constants listed in Table 2.

The load is applied according to the experimental time scale. In accordance to the measured value during the experiment, the blank-holder force is approximated as 200 kN and kept unchanged during the following forming process. The blank-holder force measured in the experiment as well as the one from the

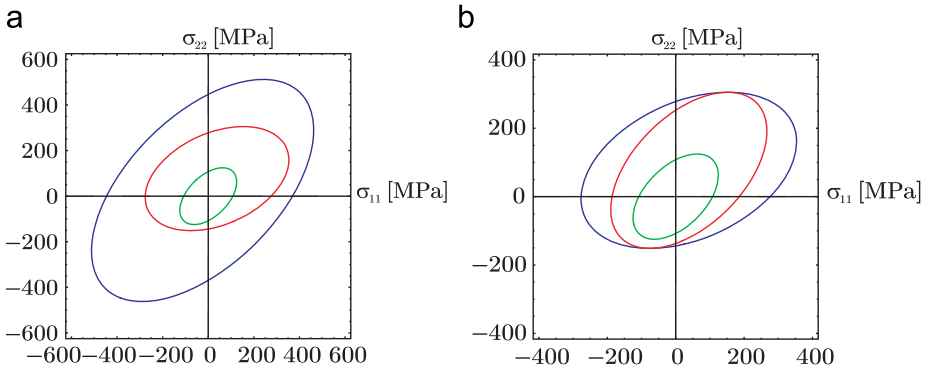

Fig. 8. a) Yield loci at the initial condition (green), at the end of plane strain tension loading (red) and at the end of simple shear loading (blue) for Iso+Kin+Cro model. b) Yield loci at the initial condition (green) and at the end of plane strain tension loading for Iso+Kin (red) and for Iso+Kin+Cro (blue) models.

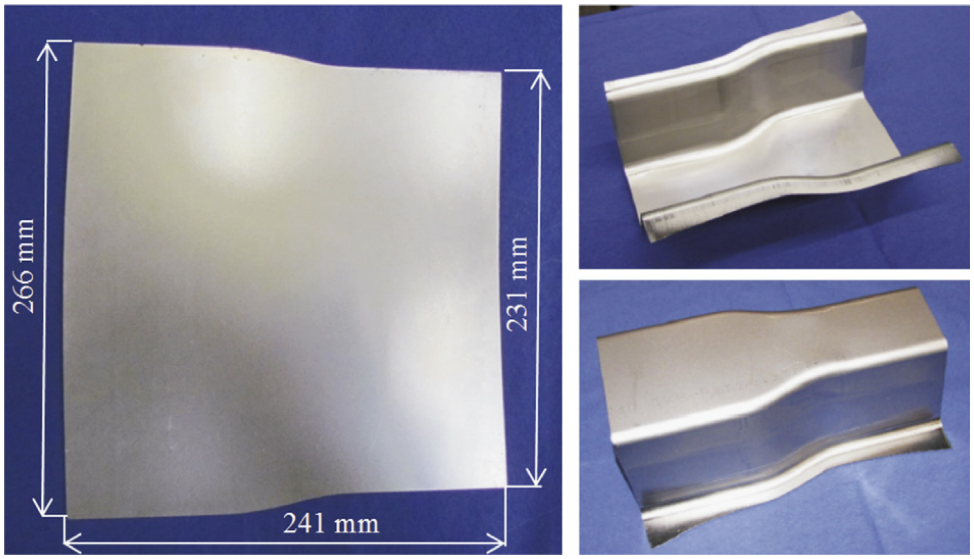

Fig. 9. Undeformed blank (left) and channel die geometry after forming (right).

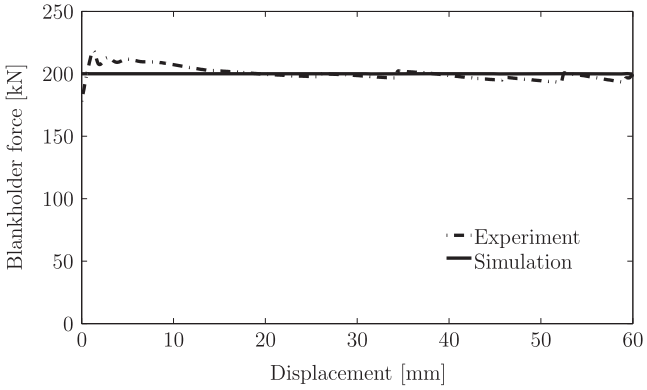

Fig. 10. Experimentally determined blank-holder force in channel forming process. The applied force in the simulation is approximated as a constant value of 200 kN.

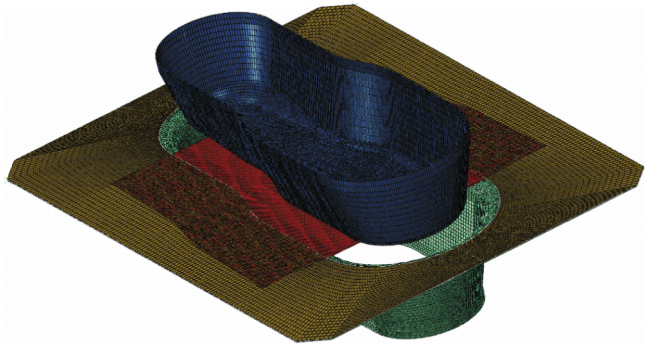

Fig. 11. Simulation set up of channel forming process.

simulation is plotted in Fig. 10. Tangential contact behavior is defined by Coulomb friction law with the friction coefficient of $\mu = 0.15$.

The simulation results of the channel forming process are shown in Figs. 12–16. First, the die force from the finite element simulation is compared to the recorded die force during the experiment (cf. Fig. 12). These two curves represent the die force versus punch displacement and an acceptable downstream following the experimental curve is observed. A local increase in the experimental die force is seen at the end of loading in Fig. 12. The tapered shape of the die may be a reason for such an increase due to the blank clamping at the end of the punch course at the upper region. This local increase of the die force is captured in the simulation, but it is less pronounced.

The geometry of the workpiece before and after spring-back, obtained from simulation, is compared to the measured experimental one in Figs. 13 and 14. An acceptable agreement between the simulation and experiment is achieved in the curved areas and the flange angles. The comparisons are presented for the both ends of the channel.

The final flange shapes, obtained from simulation and experiment, are compared in Fig. 15. Here, a small difference is seen between the two geometries. In spite of the homogeneous flange widths in the simulated one, the experimental flange shape has varying flange width especially at both ends. The non-uniform distribution of the blank-holder force in experimental process could be one reason of such difference in the flange widths. In conventional industrial problems, the main target in blank shape design is having the equal flange width all over the final part. This target decreases the required blank-holder force for controlling the wrinkling effect as well as the wasted material in final cutting.

The strain rate distribution in the workpiece at the 60% of the total forming process is shown in Fig. 16. It is observable that the

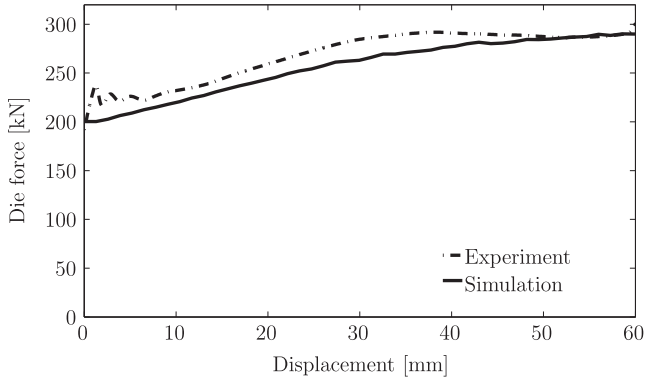

Fig. 12. Die force in the channel forming process determined in the experiment and the simulation.

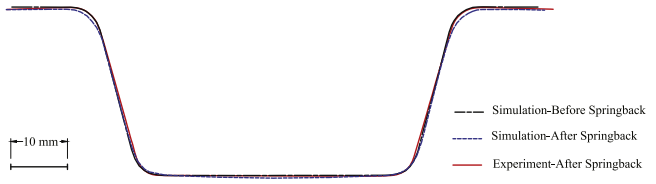

Fig. 13. Comparison of the obtained final shapes before and after spring-back from simulation with the final shapes after spring-back from experiment at wider opening end. The numerical result agrees well with the experimental data.

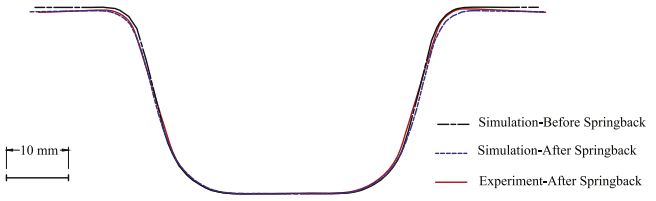

Fig. 14. Comparison of the obtained final shapes before and after spring-back from simulation with the final shapes after spring-back from experiment at narrower opening end. The numerical result is in good accordance to the experimental data.

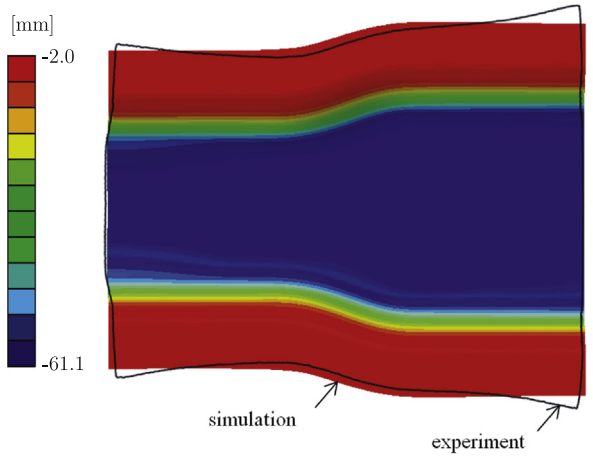

Fig. 15. Comparison of the flange shape after spring-back in the final workpiece obtained from experiment and simulation. The displacement (mm) in the z-direction is plotted.

strain rates in some areas (especially at the die edges) are considerably high – leading to a strain rate hardening effect in the material. As the sheet suddenly bends at the die edges during draw-in process, it is expected that high strain rates occur in such areas. In this regard, the strain rate values strongly depend on the die radii as well as the loading speed. The strain rate distribution

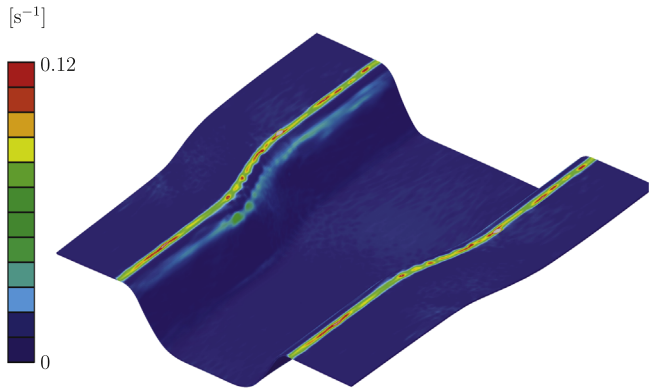

Fig. 16. Strain rate distribution after 60% of loading. The strain rates at the die edges are considerably high leading to a strain rate hardening effect in the material. Thus, the strain rate effect should be accounted for in the simulations.

shows that the strain rate effect is a phenomenon in the selected forming process which should not be neglected.

5. Conclusion

A micromechanically motivated visco-plastic material model is applied to interstitial free DC06 steel. The microstructure evolution of the material during plastic deformation is mapped via the flow potential function by an evolutionary approach. This evolutionary approach implements the change of dislocation structures parallel and orthogonal to the direction of inelastic deformation as the dynamic and the latent part of hardening via an the induced anisotropy tensor of fourth-order. This model is implemented into a VUMAT subroutine and its capabilities for taking into account the isotropic, kinematic hardening and cross hardening modes are investigated.

Considering the presented results in the one element simulation tests, the isotropic and kinematic hardening modes are successfully captured by the proposed material model. In addition, cross hardening in orthogonal loading paths is correctly predicted by the model as well. The evolution of the yield surface under the applied orthogonal loading path is depicted and the reflection of each hardening mode is well observed. In addition, the results are consistent with the microstructural hypothesis of plastic deformation in the active and the non-active slip systems, so that the cross hardening effect is clearly observed in the obtained results. The strain rate effect is successfully considered in the model via the Johnson–Cook formulation and fitted to the experimental stress–strain curves of the considered material DC06. The strain rate effect in the channel forming case study is reflected as well.

Furthermore, its applicability to an experimental channel forming process is shown. The sheet undergoes a wide range of strain paths at different locations, during the selected channel forming process with non-homogeneous section. The simulation of the selected industrial (case study) process has been carried out successfully and the obtained results are in very good agreement with the measured experimental results. Satisfactory agreement of the spring-back shape between the simulation and experiment shows that the material behavior is succeeded in modeling effective hardening mechanisms in different strain paths during the forming process.

According to the presented results the strain rate effect is an active phenomenon in the selected process and material, although the selected process is not perfect to investigate the strain rate effect in detail. Making use of this material model via the commercial finite element software ABAQUS is a practical way for precise simulating the industrial sheet forming processes. In this way, different modes of hardening consisting isotropic, kinematic and cross hardening as well as the strain rate effect are considered in the simulation of forming processes. A final word is that, the induced anisotropy is not only affecting the material behavior in non-proportional loading paths but also the product characteristics in the post production investigations (e.g., crashworthiness [46]). Therefore, even for the areas that do not experience a non-proportional loading during production, the induced anisotropy might gain importance during service-life.

Acknowledgement

Financial support for this work provided by the German Science Foundation (DFG) under contract PAK 250 (TP4) is gratefully acknowledged. The material investigations and chemical analyses provided by ThyssenKrupp Steel Europe AG are gratefully acknowledged. The Institute of Forming Technology and Lightweight Construction, Technical University of Dortmund, Germany, is thanked for conducting the channel die experiments.

Appendix A. Details of VUMAT implementation

A.1. Voigt notation

Implementation of the material models preserving tensorial forms often results in inefficient codes. For a three-dimensional application this can be remedied by the use of Voigt notation, i.e., using 6×1 vectors and 6×6 matrices for the representation of symmetric second-order tensors and fourth-order tensors with at least minor-symmetries. This allows application of standard matrix algebra.

The 6×1 vector representations for the strain tensor is $\mathbf{E}=[E_{11},E_{22},E_{33},2E_{12},2E_{23},2E_{13}]^{\top}$ where the strain tensor norm $|\mathbf{E}|=\sqrt{E_{ij}E_{ij}}$ is computed using $|\mathbf{E}|=\sqrt{\mathbf{E}^{\top}\mathbb{Q}\mathbf{E}}$, with

$$\mathbb{Q}=\frac{1}{2}\left[\begin{array}{ccc|ccc} 2&0&0&0&0&0\\ 0&2&0&0&0&0\\ 0&0&2&0&0&0\\ \hline 0&0&0&1&0&0\\ 0&0&0&0&1&0\\ 0&0&0&0&0&1 \end{array}\right] \tag{A.1}$$

All the strain and strain-like tensors follow the stencil $[1|2]^{\top}$, where the shear continuum components are multiplied by two

$$\left.\begin{array}{l} \mathbf{E}^{e}=[E^{e}_{11},E^{e}_{22},E^{e}_{33},2E^{e}_{12},2E^{e}_{23},2E^{e}_{13}]^{\top},\\ \mathbf{E}^{p}=[E^{p}_{11},E^{p}_{22},E^{p}_{33},2E^{p}_{12},2E^{p}_{23},2E^{p}_{13}]^{\top},\\ \mathbf{N}^{p}=[N^{p}_{11},N^{p}_{22},N^{p}_{33},2N^{p}_{12},2N^{p}_{23},2N^{p}_{13}]^{\top}. \end{array}\right\} \tag{A.2}$$

The 6×1 vector representations for the stress and stress-like tensors follow the stencil $[1|1]^{\top}$, where the shear continuum components are multiplied by unity

$$\left.\begin{array}{l} \mathbf{S}=[S_{11},S_{22},S_{33},S_{12},S_{23},S_{13}]^{\top},\\ \mathbf{X}=[X_{11},X_{22},X_{33},X_{12},X_{23},X_{13}]^{\top}, \end{array}\right\} \tag{A.3}$$

where the tensor norm, e.g., $|\mathbf{S}|=\sqrt{S_{ij}S_{ij}}$, is computed using $|\mathbf{S}|=\sqrt{\mathbf{S}^{\top}\mathbb{Q}^{-1}\mathbf{S}}$.

A similar distinction also applies for the 6×6 matrix representations of the fourth-order tensors acting on the stress-like or strain-like tensors. Hence while representing $\mathbf{E}^e:\mathbb{C}:\mathbf{E}^e$ as $[\mathbf{E}^e]^\top\mathbb{C}\mathbf{E}^e$, the matrix form of $\mathbb{C}=\mathbb{C}^{\mathrm{T}}$ reads

$$\mathbb{C}=\left[\begin{array}{ccc|ccc} C_{1111} & C_{1122} & C_{1133} & C_{1112} & C_{1123} & C_{1113} \\ C_{2211} & C_{2222} & C_{2233} & C_{2212} & C_{2223} & C_{2213} \\ C_{3311} & C_{3322} & C_{3333} & C_{3312} & C_{3323} & C_{3313} \\ \hline C_{1211} & C_{1222} & C_{1233} & C_{1212} & C_{1223} & C_{1213} \\ C_{2311} & C_{2322} & C_{2333} & C_{2312} & C_{2323} & C_{2313} \\ C_{1311} & C_{1322} & C_{1333} & C_{1312} & C_{1323} & C_{1313} \end{array}\right]. \tag{A.4}$$

Hence, the stencil $\left[\begin{array}{c|c} 1 & 1 \\ \hline 1 & 1 \end{array}\right]$ is used over the continuum components. Note that with Eqs. (A.3) and (A.4), the stress definition in Eq. (3) naturally replaces with its corresponding Voigt form

$$\mathbf{S}=\mathbb{C}\mathbf{E}^e, \tag{A.5}$$

and hence $[\mathbf{E}^e]^\top\mathbb{C}\mathbf{E}^e=[\mathbf{E}^e]^\top\mathbf{S}=[\mathbf{S}]^\top\mathbf{E}^e$.

While representing the expression $[\mathbf{S}-\mathbf{X}]:[\mathbb{A}+\mathbb{H}]:[\mathbf{S}-\mathbf{X}]$, as $[\mathbf{S}-\mathbf{X}]^\top[\mathbb{A}+\mathbb{H}][\mathbf{S}-\mathbf{X}]$ the matrix form of $\mathbb{A}$ and $\mathbb{H}$, which preserve both major- and minor-symmetries with $A_{ijkl}=A_{jikl}=A_{ijlk}=A_{klij}$ and $H_{ijkl}=H_{jikl}=H_{ijlk}=H_{klij}$, read

$$\mathbb{A}=\left[\begin{array}{ccc|ccc} A_{1111} & A_{1122} & A_{1133} & 2A_{1112} & 2A_{1123} & 2A_{1113} \\ A_{2211} & A_{2222} & A_{2233} & 2A_{2212} & 2A_{2223} & 2A_{2213} \\ A_{3311} & A_{3322} & A_{3333} & 2A_{3312} & 2A_{3323} & 2A_{3313} \\ \hline 2A_{1211} & 2A_{1222} & 2A_{1233} & 4A_{1212} & 4A_{1223} & 4A_{1213} \\ 2A_{2311} & 2A_{2322} & 2A_{2333} & 4A_{2312} & 4A_{2323} & 4A_{2313} \\ 2A_{1311} & 2A_{1322} & 2A_{1333} & 4A_{1312} & 4A_{1323} & 4A_{1313} \end{array}\right], \tag{A.6}$$

and

$$\mathbb{H}=\left[\begin{array}{ccc|ccc} H_{1111} & H_{1122} & H_{1133} & 2H_{1112} & 2H_{1123} & 2H_{1113} \\ H_{2211} & H_{2222} & H_{2233} & 2H_{2212} & 2H_{2223} & 2H_{2213} \\ H_{3311} & H_{3322} & H_{3333} & 2H_{3312} & 2H_{3323} & 2H_{3313} \\ \hline 2H_{1211} & 2H_{1222} & 2H_{1233} & 4H_{1212} & 4H_{1223} & 4H_{1213} \\ 2H_{2311} & 2H_{2322} & 2H_{2333} & 4H_{2312} & 4H_{2323} & 4H_{2313} \\ 2H_{1311} & 2H_{1322} & 2H_{1333} & 4H_{1312} & 4H_{1323} & 4H_{1313} \end{array}\right], \tag{A.7}$$

with $\mathbb{A}=\mathbb{A}^{\mathrm{T}}$ and $\mathbb{H}=\mathbb{H}^{\mathrm{T}}$. Hence, the stencil $\left[\begin{array}{c|c} 1 & 2 \\ \hline 2 & 4 \end{array}\right]$ applies over the continuum components. This notation leads to the following matrix form of the Hill-48-type structural matrix:

$$\mathbb{A}=\left[\begin{array}{cccccc} G+H & -H & -G & 0 & 0 & 0 \\ -H & F+H & -F & 0 & 0 & 0 \\ -G & -F & F+G & 0 & 0 & 0 \\ 0 & 0 & 0 & 2N & 0 & 0 \\ 0 & 0 & 0 & 0 & 2L & 0 \\ 0 & 0 & 0 & 0 & 0 & 2M \end{array}\right]. \tag{A.8}$$

Note that with Eqs. (A.8) and (A.7), the flow rule in Eq. (8) naturally replaces with its corresponding Voigt form

$$\mathbf{E}^p/\dot{e}^p=\frac{[\mathbb{A}+\mathbb{H}][\mathbf{S}-\mathbf{X}]}{\sqrt{[\mathbf{S}-\mathbf{X}]^\top[\mathbb{A}+\mathbb{H}][\mathbf{S}-\mathbf{X}]}}.$$

The Voigt representation of the tensorial expressions which uses different types in each side of the equation, like in Eq. (12), needs additional transformation operators. For example the Voigt form of Eq. (12) reads $\dot{\mathbf{X}}/\dot{e}^p=c_x[s_x\mathbb{Q}\mathbf{N}^p-\mathbf{X}]$, where $\mathbf{N}^p=\dot{\mathbf{E}}^p/|\dot{\mathbf{E}}^p|$.

The matrix representation of the Eq. (13) is given as

$$\dot{\mathbb{H}}/\dot{e}^p=c_d[s_d\mathbf{N}^p[\mathbf{N}^p]^\top-\mathbb{H}^d]+c_l[s_l[\mathbf{N}^p[\mathbf{N}^p]^\top-\mathbb{I}^{\mathrm{dev}}]-\mathbb{H}^l], \tag{A.9}$$

where

$$\mathbf{N}^p\cdot[\mathbf{N}^p]^\top=\left[\begin{array}{ccc|ccc} N_{11}^pN_{11}^p & N_{11}^pN_{22}^p & N_{11}^pN_{33}^p & 2N_{11}^pN_{12}^p & 2N_{11}^pN_{23}^p & 2N_{11}^pN_{13}^p \\ N_{22}^pN_{11}^p & N_{22}^pN_{22}^p & N_{22}^pN_{33}^p & 2N_{22}^pN_{12}^p & 2N_{22}^pN_{23}^p & 2N_{22}^pN_{13}^p \\ N_{33}^pN_{11}^p & N_{33}^pN_{22}^p & N_{33}^pN_{33}^p & 2N_{33}^pN_{12}^p & 2N_{33}^pN_{23}^p & 2N_{33}^pN_{13}^p \\ \hline 2N_{12}^pN_{11}^p & 2N_{12}^pN_{22}^p & 2N_{12}^pN_{33}^p & 4N_{12}^pN_{12}^p & 4N_{12}^pN_{23}^p & 4N_{12}^pN_{13}^p \\ 2N_{23}^pN_{11}^p & 2N_{23}^pN_{22}^p & 2N_{23}^pN_{33}^p & 4N_{23}^pN_{12}^p & 4N_{23}^pN_{23}^p & 4N_{23}^pN_{13}^p \\ 2N_{13}^pN_{11}^p & 2N_{13}^pN_{22}^p & 2N_{13}^pN_{33}^p & 4N_{13}^pN_{12}^p & 4N_{13}^pN_{23}^p & 4N_{13}^pN_{13}^p \end{array}\right], \tag{A.10}$$

and

$$\mathbb{I}^{\mathrm{dev}}=\frac{1}{3}\left[\begin{array}{ccc|ccc} 2 & -1 & -1 & 0 & 0 & 0 \\ -1 & 2 & -1 & 0 & 0 & 0 \\ -1 & -1 & 2 & 0 & 0 & 0 \\ \hline 0 & 0 & 0 & 6 & 0 & 0 \\ 0 & 0 & 0 & 0 & 6 & 0 \\ 0 & 0 & 0 & 0 & 0 & 6 \end{array}\right]. \tag{A.11}$$

Finally, the matrix form of $\mathbb{H}^d$ reads $\mathbb{H}^d=[[\mathbb{Q}\mathbf{N}^p]^\top\mathbb{H}[\mathbb{Q}\mathbf{N}^p]]\,[\mathbf{N}^p[\mathbf{N}^p]^\top]$.

A.2. Algorithm

The staggered algorithmic treatment of the material model implementation is summarized in Algorithm 1. This approach shows required accuracy with sufficiently small stable time steps adapted in the dynamic-explicit finite element code.

Algorithm 1. Algorithmic treatment of the framework.

1. Initialize the matrix form of the structural tensor for the induced anisotropy with the 6×6 zero matrix $\mathbb{O}$:
   $\mathbb{O}\longrightarrow\mathbb{H}$.
2. For the given strain increment $\Delta\mathbf{E}$ compute the elastic trial state:
   $$\begin{array}{r}\Delta\mathbf{E}\longrightarrow\Delta\mathbf{E}^e,\\ \mathbf{S}+\mathbb{C}\Delta\mathbf{E}^e\longrightarrow\mathbf{S},\\ \sqrt{[\mathbf{S}-\mathbf{X}]^\top[\mathbb{A}-\mathbb{H}][\mathbf{S}-\mathbf{X}]}-\sigma_y(e^p,\dot{e}^p)\longrightarrow\phi^p.\end{array}$$
3. **IF** $\phi^p<0$ **THEN GOTO 4**.
   ELSE GOTO 5.
4. **Elastic Step**: Trial step does not need correction. **GOTO 2**.
5. **Elasto-Plastic Step:** Trial step needs correction. Apply the cutting-plane return mapping algorithm to update the elastic and inelastic solution dependent state variables including the equivalent plastic strain increment Δe^p and the plastic strain increment $\Delta\mathbf{E}^p$ for $\dot{\mathbb{H}}=\mathbb{O}$.
6. Compute the normal $\mathbf{N}^p$ in the plastic flow direction:
   $\Delta\mathbf{E}^p/|\Delta\mathbf{E}^p|\longrightarrow\mathbf{N}^p$.
7. Integrate $\mathbb{H}$ with the incremental form of Eq. (A.9):
   $$\begin{array}{r}[[\mathbb{Q}\mathbf{N}^p]^\top\mathbb{H}[\mathbb{Q}\mathbf{N}^p]]\;[\mathbf{N}^p[\mathbf{N}^p]^\top]\longrightarrow\mathbb{H}^d\\ \mathbb{H}-\mathbb{H}^d\longrightarrow\mathbb{H}^l\\ c_d[s_d\mathbf{N}^p[\mathbf{N}^p]^\top-\mathbb{H}^d]\Delta e^p\longrightarrow\Delta\mathbb{H}^d,\\ c_l[s_l[\mathbf{N}^p[\mathbf{N}^p]^\top-\mathbb{I}^{\mathrm{dev}}]-\mathbb{H}^l]\Delta e^p\longrightarrow\Delta\mathbb{H}^l,\\ \Delta\mathbb{H}^d+\Delta\mathbb{H}^l\longrightarrow\Delta\mathbb{H},\\ \mathbb{H}+\Delta\mathbb{H}\longrightarrow\mathbb{H}.\end{array}$$
8. **GOTO 2.**

References

[1] Bauschinger J. Über die Veränderung der Elasticitätsgrenze und des Elasticitätsmoduls verschiedener Metalle. Zivilingenieur 1881;27:289–348.
[2] Ghosh AK, Backofen WA. Strain hardening and instability in biaxially streched sheets. Metall Trans 1973;4(4):1113–23.
[3] Rauch EF, Schmitt JH. Dislocation substructures in mild steel deformed in simple shear. Mater Sc Eng A 1989;113:441–8.
[4] Rauch EF, Thuillier S. Rheological behaviour of mildsteel under monotonic loading conditions and cross-loading. Mater Sc Eng A 1993;164:255–9.
[5] Nesterova E, Bacroix B, Teodosiu C. Experimental observation of microstructure evolution under strain-path changes in low-carbon IF steel. Mater Sci Eng A 2001;309–310(0):495–9 [Dislocations 2000: an International conference on the fundamentals of plastic deformation].
[6] Gardey B, Bouvier S, Richard V, Bacroix B. Texture and dislocation structures observation in a dual-phase steel under strain-path changes at large deformation. Mater Sci Eng. A 2005;400–401(0):136–41.
[7] Kalidini SR, Bronkhorst CA, Anand L. Crystallographic texture evolution during bulk deformation processing of fcc metals. J Mech Phys Solids 1992;40:537–69.
[8] Marin EB, Dawson PR. On modelling the elasto-viscoplastic response of metals using polycrystal plasticity. Comput Methods Appl Mech Eng 1998;165(1-4):23–41.
[9] Holmedal B, van Houtte P, An Y. A crystal plasticity model for strain-path changes in metals. Int J Plast 2008;24(8):702–7.
[10] Roters F, Eisenlohr P, Hantcherli L, Tjahjanto D, Bieler T, Raabe D. Overview of constitutive laws, homogenization and multiscale methods in crystal plasticity finite-element modeling: theory, experiments, applications. Acta Mater 2010;58(4):1152–211.
[11] Anand L, Gurtin ME, Lele SP, Gething C. A one-dimensional theory of strain-gradient plasticity: formulation, numerical results. J Mech Phys Solids 2005;53:1789–826.
[12] Bardella L. A deformation theory of strain gradient crystal plasticity that accounts for geometrically necessary dislocations. J Mech Phys Solids 2006;54:128–60.
[13] Bargmann S, Svendsen B, Ekh M. An extended crystal plasticity model for latent hardening in polycrystals. Comput Mech 2011;48:631–48.
[14] Evers LP, Brekelmans WAM, Geers MGD. Scale dependent crystal plasticity framework with dislocation density and grain boundary effects. Int J Solids Struct 2004;41:5209–30.
[15] Husser E, Bargmann S, Lilleodden E. Computational modeling of intrinsically induced strain gradients during compression of *c*-axis oriented magnesium single crystal. Acta Mater 2014;71:206–19.
[16] Ohno N, Okumura D. Higher-order stress and grain size effects due to self-energy of geometrically necessary dislocations. J Mech Phys Solids 2007;55:1879–98.
[17] Kurtyka T, Zyczkowski M. Evolution equation for distortional plastic hardening. Int J Plast 1996;12(2):81–98.
[18] Baltov A, Sawczuk A. A rule of anisotropic hardening. ACTA Mech 2012;1(2):81–92.
[19] Levkovitch V, Svendsen B. Accurate hardening modeling as basis for the realistic simulation of sheet forming processes with complex strain-path change. In: J. Cesar de Sa, editor. 9th international conference on numerical methods in industrial forming processes (NUMIFORM 2007), Porto, Portugal, vol. 2. AIP Conference Proceedings; 2007. p. 1331–6.
[20] Clausmeyer T, van den Boogaard H, Noman M, Gershteyn M, Schaper M, Svendsen B, et al. Phenomenological modeling of anisotropy induced by evolution of the dislocation structure on the macroscopic and microscopic scale. Int J Mater Form 2011;4(2):141–54.
[21] Pietryga MP, Vladimirov IN, Reese S. A finite deformation model for evolving flow anisotropy with distortional hardening including experimental validation. Mech Mater 2012;44(0):163–73.
[22] Barthel C, Klusemann B, Denzer R, Svendsen B. Modeling of a thermomechanical process chain for sheet steels. Int J Mech Sci 2013;74:46–54.
[23] Barlat F, Ha J, Gracio JJ, Lee MG, Rauch EF, Vincze G. Extension of homogeneous anisotropic hardening model to cross-loading with latent effects. Int J Plast 2013;46:130–42.
[24] Teodosiu C, Hu Z. Evolution of the intragranular microstructure at moderate and large strains: modelling and computational significance. In: Shen S, Dawson P, editors. Simulation of materials processing: theory, methods and applications. Rotterdam: Balkema; 1995. p. 173–82.
[25] Hiwatashi S, van Bael A, van Houtte P, Teodosiu C. Modelling of plastic anisotropy based on texture and dislocation structure. Comput Mater Sci 1997;9:274–84.
[26] Haddadi H, Bouvier S, Banu M, Maier C, Teodosiu C. Modelling of plastic anisotropy based on texture and dislocation structure. Int J Plast 2006;22(12):2226–71.
[27] Li S, Hoferlin E, van Bael A, van Houtte P, Teodosiu C. Finite element modeling of plastic anisotropy induced by texture and strain-path change. Int J Plast 2003;19(5):647–74.
[28] Wang J, Levkovitch V, Reusch F, Svendsen B, Huetink J, van Riel M. On the modeling of hardening in metals during non-proportional loading. Int J Plast 2008;24(6):1039–70.
[29] Uenishi A, Teodosiu C. Constitutive modelling of the high strain rate behaviour of interstitial-free steel. Int J Plast 2004;20(4–5):915–36.
[30] Feigenbaum HP, Dafalias YF. Directional distortional hardening in metal plasticity within thermodynamics. Int J Solids Struct 2007;44:7526–42.
[31] Feigenbaum HP, Dafalias YF. Simple model for directional distortional hardening in metal plasticity within thermodynamics. ASCE J Eng Mech 2008;134(9):730–8.
[32] Plesek J, Feigenbaum HP, Dafalias YF. Convexity of yield surface with directional distortional hardening rules. ASCE J Eng Mech 2010;136(4):477–84.
[33] Hill R. A theory of the yielding and plastic flow of anisotropic metals. Proc Roy Soc Lond 1948;193:281–97.
[34] Larour P. Strain rate sensitivity of automotive sheet steels: influence of plastic strain, strain rate, temperature, microstructure, bake hardening and pre-strain. RWTH Aachen University, 2010. ISBN 978-3-8322-9149-5.
[35] van Riel M. Strain path dependency in sheet metal – experiments and models [Ph.D.Thesis]. Twente University, 2009.
[36] Clausmeyer T, Gerstein G, Bargmann S, Svendsen B, van den Boogaard H, Zillmann B. Experimental characterization of microstructure development during loading path changes in bcc sheet steels. J Mater Sci 2013;48(2):674–89.
[37] Husser E, Clausmeyer T, Gershteyn G, Bargmann S. Determination of average dislocation densities in metals by analysis of digitally processed tem images. Mater Sci Eng Technol 2013;44(6):541–6.
[38] Hosford W. A generalized isotropic yield criterion. J Appl Mech Trans ASME Eng 1972;39:607–9.
[39] Karafillis A, Boyce M. A general anisotropic yield criterion using bounds and a transformation weighting tensor. J Mech Phys Solids 1993;41:1859–86.
[40] Barlat F, Lege D, Brem J. A six component yield function for anisotropic materials. Int J Plast 1991;7:693–712.
[41] Johnson G, Cook W. A constitutive model and data for metals subjected to large strains, high strain rates and high temperatures. In: Proceedings of the 7th international symposium on ballistics, The Hague; 1983. p. 541—7.
[42] Wang W, Sluys L, de Borst R. Viscoplasticity for instabilities due to strain softening and strain-rate softening. Int J Numer Methods Eng 1997;40:3839–64.
[43] Lee M, Kim D, Kim C, Wenner M, Wagoner R, Chung K. A practical two-surface plasticity model and its application to spring-back prediction. Int J Plast 2007;23:1189–212.
[44] van Riel M, van den Boogaard H. Stress–strain responses for continuous orthogonal strain path changes with increasing sharpness. Scr Mater 2007;57(5):381–4.
[45] Witulski J, Trompeter M, Tekkaya E. Coated polymers for rapid tooling of deep drawing tools. In: Proceedings of the 2nd international conference process machine interactions, vol. 57, issue 5, Vancouver, BC, Canada; 10th–11th June 2010. p. 381–4.
[46] Steglich D, Bohlen J, Tian X, Riekehr S, Kashaev N, Bargmann S, et al. Crashworthiness of magnesium sheet structures. In: Stone I, McKay B, Fan ZY, editors, 6th international light metals technology conference on light metals technology 2013 (LMT 2013), Materials Science Forum, vol. 765, Brunel University, BCAST, Old Windsor, England; 24–26 July 2013. p. 590–4.